# Supplementary Information: Giant exchange splitting in the electronic structure of A-type 2D antiferromagnet CrSBr

Matthew D. Watson,[1,*] Swagata Acharya,[2] James E. Nunn,[1,3] Laxman Nagireddy,[3,4,5] Dimitar Pashov,[6] Malte Rösner,[7] Mark van Schilfgaarde,[2] Neil R. Wilson,[3] and Cephise Cacho[1]

[1]*Diamond Light Source Ltd, Harwell Science and Innovation Campus, Didcot, OX11 0DE, UK*
[2]*National Renewable Energy Laboratory, Golden 80401 CO, USA*
[3]*Department of Physics, University of Warwick, Coventry, CV4 7AL, UK*
[4]*CY Cergy Paris Université, CEA, LIDYL, 91191 Gif-sur-Yvette, France*
[5]*Université Paris-Saclay, CEA, LIDYL, 91191, Gif-sur-Yvette, France*
[6]*Theory and Simulation of Condensed Matter, King's College London, The Strand, London WC2R2LS, UK*
[7]*Institute for Molecules and Materials, Radboud University, Heijendaalseweg 135, 6525AJ Nijmegen, The Netherlands*

(Dated: June 7, 2024)

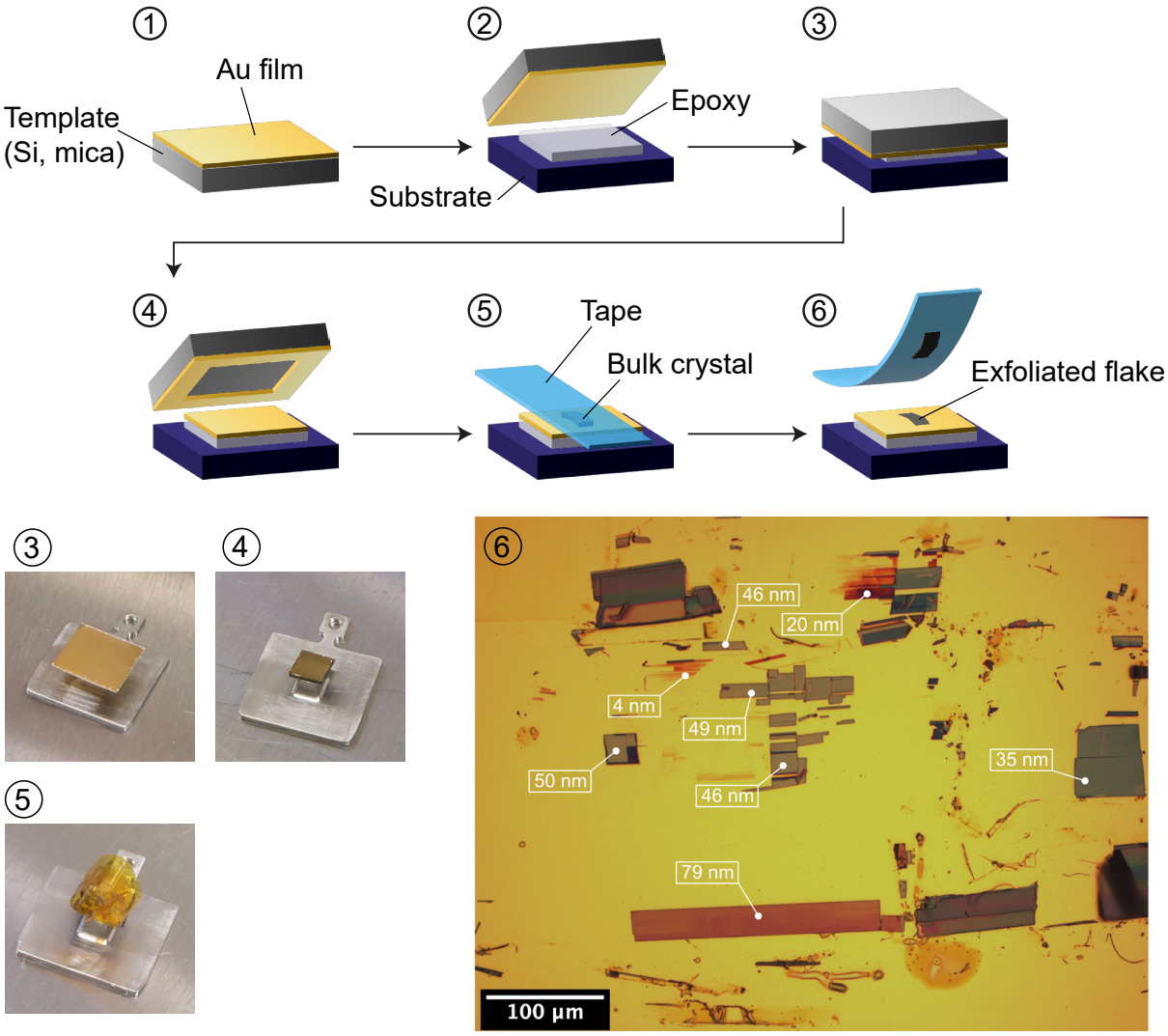


Supplementary Figure 1. **Illustration of template-stripped Au methodology.** (1) First, gold is deposited onto Si or mica. In the case of mica, it is freshly cleaved before deposition. (2,3) The Au film is then glued to a substrate (Si chip) face down, using an epoxy (Opti-tecTM 5054-1 High Temperature Epoxy Adhesive). (4) After the epoxy is cured, the mica is cleaved off, in an Argon glove box. The bond between the epoxy and the Au film is stronger than between the Au film and the flat mica surface, so the Au film stays with the substrate. The freshly-exposed top surface inherits the minimal surface roughness of the template. (5) Still in the glove box, and shortly after the previous step, a bulk crystal of CrSBr is exfoliated and the tape is put onto the Au. This is then transferred to the load lock of the UHV system, minimizing exposure to air. (6) Once the load lock is pumped down to a pressure of $\sim 2\times10^{-8}$ mbar, the tape is removed (using a hook on an in-vacuum wobble stick) and the sample is transferred immediately to the measuring chamber with a pressure of $1 \times 10^{-10}$ mbar. When the gold had been prepared correctly, we found suitable flakes for measuring (i.e. sharp bands and no charging) with around 75% probability. Final image: Optical micrograph of CrSBr exfoliated onto TSG from silicon. CrSBr flakes of various thickness are apparent against the gold background, with the colour of the flakes changing with thickness. Some of the flakes are labelled with their thickness as measured by atomic force microscopy. Within this region there are several flakes of 10s of nm thickness, and 10s of $\mu$m lateral dimensions, that would be suitable for $\mu$ARPES

.

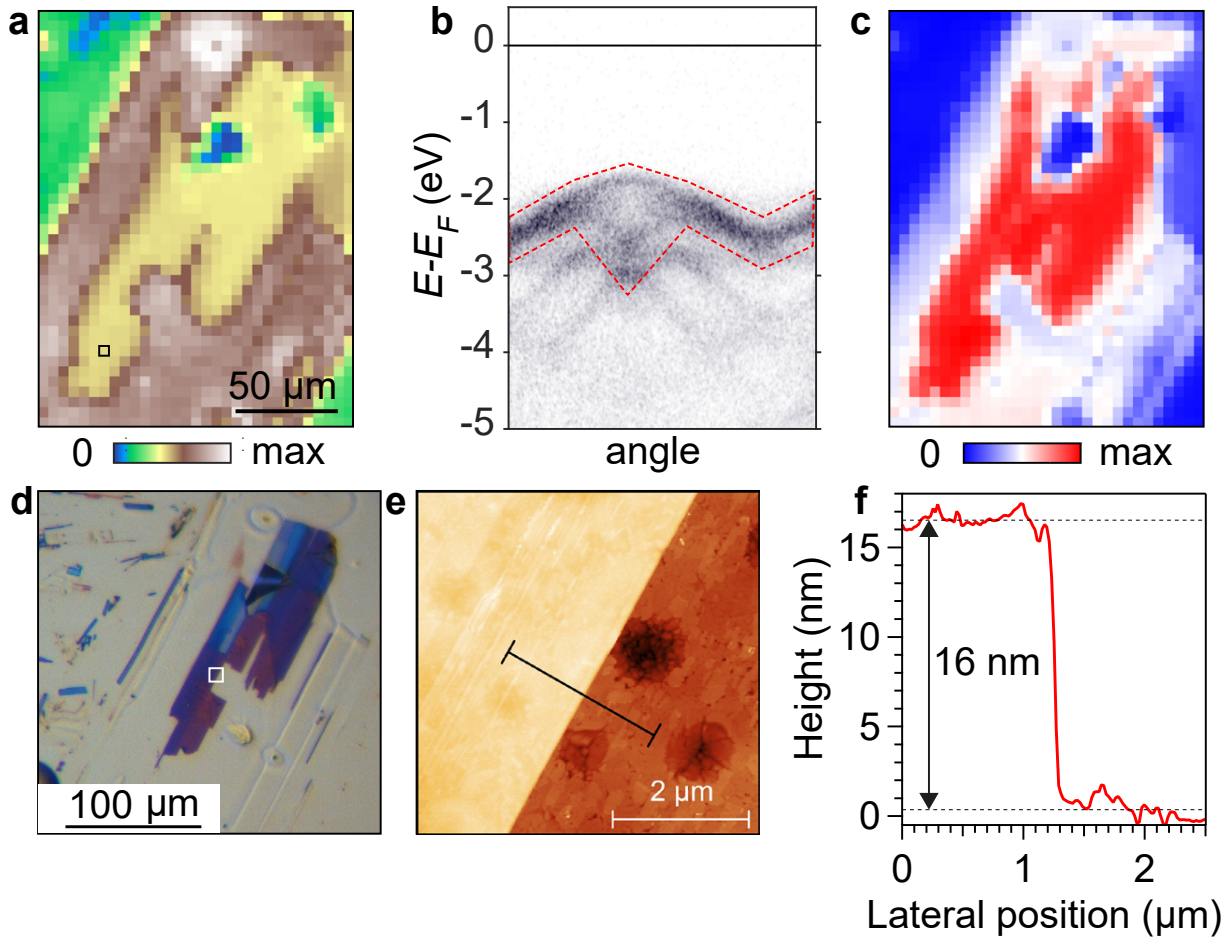


Supplementary Figure 2. **SPEM and AFM**. (a) SPEM (total counts) image of a typical sample. (b) ARPES data from the outlined pixel. The energy scale of the data is referenced to $E_F$, the Fermi level of the gold, as opposed to $E_{vb}$ which is the convention used throughout the main text. The dotted red line shows the polygon ROI used to filter the data for (c), an map of intensity on the Cr bands of the CrSBr. (d) Optical microscope image of this part of the sample, and (e,f) AFM measurement confirming a step height of 16 nm between the template-stripped gold and the flake of CrSBr at the position indicated by the white square in (d). The c-axis lattice constant is 0.7934 nm so this corresponds to $\approx 20$ layers. However, the constrast in the optical image varies substantially without noticeable effect on the measured ARPES spectra, indicating that there is a reasonable tolerance on the thickness of the sample that can be measured without encountering sample charging issues. Note however that the dark blue triangle found towards the top right corner of the optical image in is likely a flake which is lifted away from the gold substrate, and in this region we find near-zero counts, presumably due to strong charging.

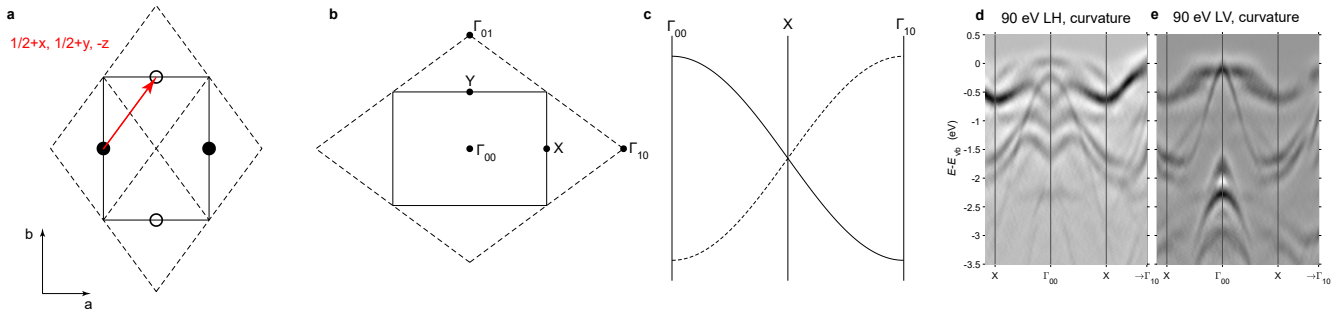


Supplementary Figure 3. **Effect of glide-mirror symmetry on ARPES measurements.** (a) Representation of the real-space unit cell of CrSBr (solid line), with 2 Cr per unit cell, projected into the $ab$ plane. Only the Cr atoms are shown, with those above and below the plane marked with filled and open symbols respectively. Red text and arrow highlights the $n$ glide-mirror symmetry under which all Cr atoms are equivalent. Dashed line shows an effective 1-Cr unit cell that would be applicable if the structure was collapsed along z. (b) The crystallographic Brillouin zone of CrSBr (solid lines) and the effective "unfolded" Brillouin zone corresponding to the 1-Cr unit cell. (c) Effect of the glide symmetry on band dispersions. For each dispersion that would exist in the unfolded 1-Cr Brillouin zone, a second copy is backfolded in the crystallographic 2-Cr Brillouin zone, however there is no interaction at the X point (or equivalently Y point), where there are symmetry-enforced band degeneracies. (d) ARPES measurements (LH data same as Fig. 3 of main text), presented as curvature analysis to highlight weaker features. The ARPES intensity in a high symmetry geometry with a given linear light polarisation follows only one of the two glide-equivalent branches. As a result the X point does not appear to the eye to be a point of high-symmetry in the raw data, but it is when one considers the band dispersions (rather than intensities) and all polarisations of light. Moreover, the ARPES intensity at $\Gamma_{10}$ or $\Gamma_{01}$ (that is, the next $\Gamma$ points along $k_x$ and $k_y$ respectively) will be quite different to that at $\Gamma_{00}$ (normal emission).
The consideration of non-symmorphic space group symmetries in the context of ARPES has a long history [1–3]. A contemporary analogy is the known effect of in-plane $n$-glide-mirror symmetry in Fe-based superconductors [4], where for example the selection rules for the $d_{xz}/d_{yz}$-derived hole pockets reverse at the second $\Gamma$ points. Similarly, apparently alternating selection rules were seen in Fig. 6 of Bianchi *et al.* [5], where their measurement geometry allowed them to reach multiple $\Gamma$ points. (Note that Bianchi et al. also used reversed notation, i.e. their $\Gamma_{01}$ is equivalent to our $\Gamma_{10}$.)

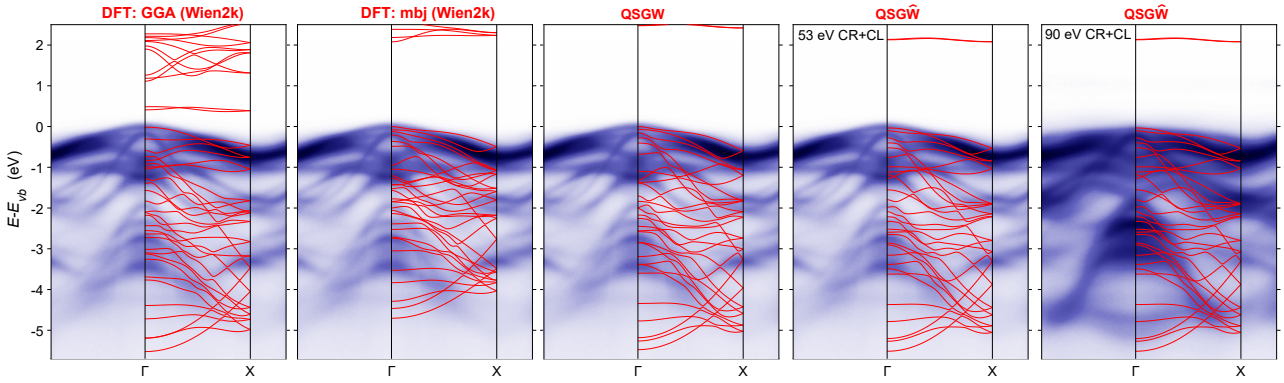


Supplementary Figure 4. **Comparison of bands calcuated with different *ab initio* approaches to measured dispersions along $\Gamma$-X.** From left to right, the calculations are: "vanilla" DFT (GGA, Wien2k [6]); the modified Becke-Johnson (mBJ) potential (mBJ potential with LDA correlation [7], Wien2k); QSGŴ; QSGŴ. The vanilla DFT (GGA) gives a clearly absurd band gap. The mBJ calculation gives a more reasonable band gap, but the valence band dispersions match badly, and the conduction band structure is likely unphysical. The QSGW (i.e. without ladder diagrams) gives a reasonable agreement for the valence bands and also a large band gap, however the QSGŴ yields improved agreement, also reducing the band gap a little. In particular, near X points the QSGŴ bands pinch closer together into more discrete manifolds, and the lowest of the Cr $t_{2g}$ bands is much more flat, which are features also seen in the data. The ARPES data in the first 4 panels is measured with 53 eV CR+CL (same as Fig. 2(b) in main text), and the final panel is 90 eV CR+CL, which highlights some other bands which are weak in the 53 eV data, but still well-reproduced by the QSGŴ calculation.

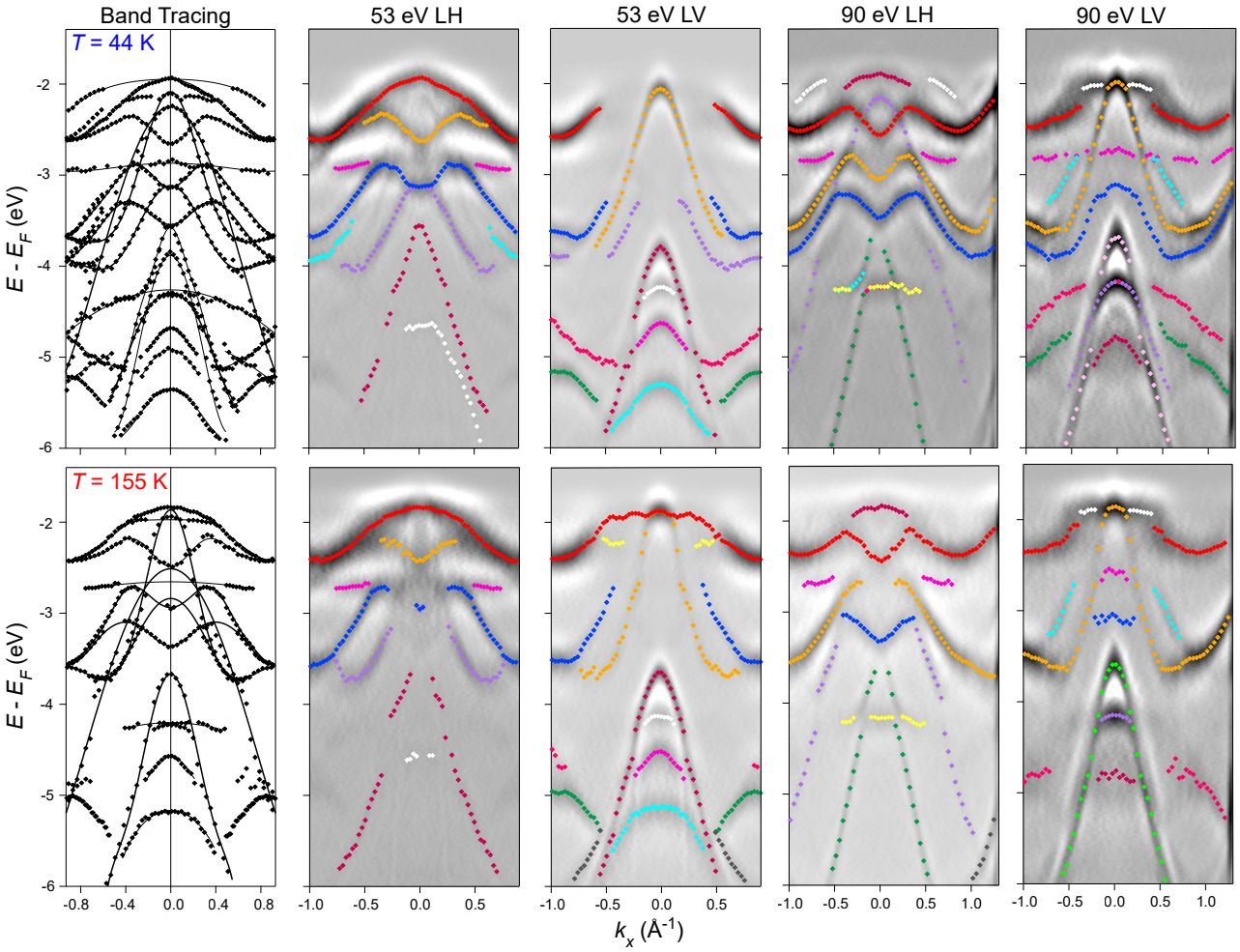


Supplementary Figure 5. **Band tracing procedure.** The band tracing was based on four data sets at each temperature (44 K, top row, and 155 K, bottom row), namely measurements at 53 eV and 90 eV in both LH and LV light polarisations. The energy scale here is referenced to the Fermi level. The curvature of the data is plotted, from which band positions were extracted according to the following procedure. The band tracing was obtained by analysing independently each curvature data for 2 photon energies and 2 polarisation (LH/LV). To reduce the curvature noise the k axis was rebinned to $\Delta k$=0.04 $\text{Å}^{-1}$. The band positions was extracted by identifying the half-maximum position of curvature peaks along the energy axis. The positions obtained were than manually cross-checked with the curvature image. Certain features which are consistently found in all 4 measurements were used to correct any minor energy drift between the different energies and polarisations.

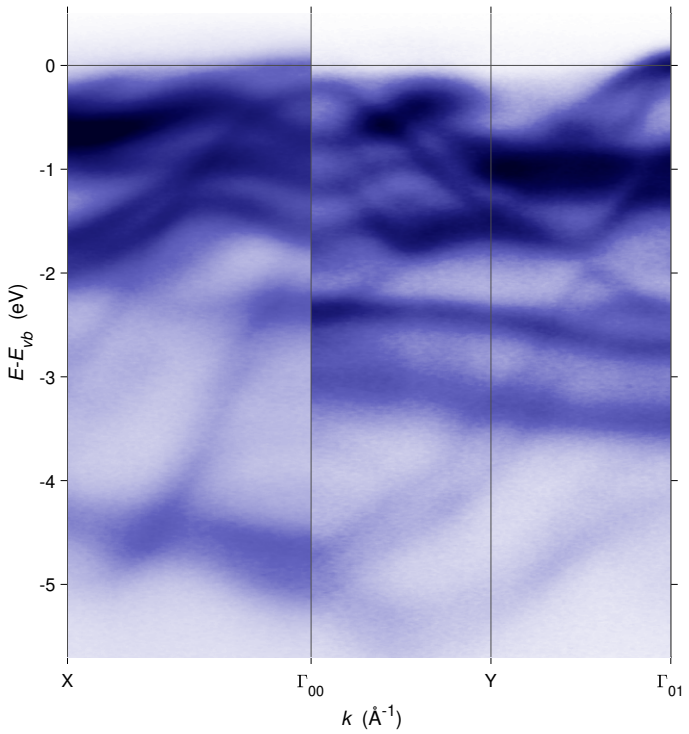


Supplementary Figure 6. **X-$\Gamma_{00}$-Y-$\Gamma_{01}$ dispersion**. While we focused on the dispersion along Γ-X in the main text, here we also present the dispersion along a path $\Gamma_{00}$-Y-$\Gamma_{01}$, stitched from two different samples. The light polarisation is LH in both cases, but the crystal is rotated by 90 degrees. Note that the glide symmetry affects the intensity along $\Gamma_{00}$-Y-$\Gamma_{01}$ in the same way as $\Gamma_{00}$-X-$\Gamma_{10}$, as shown in SI3.

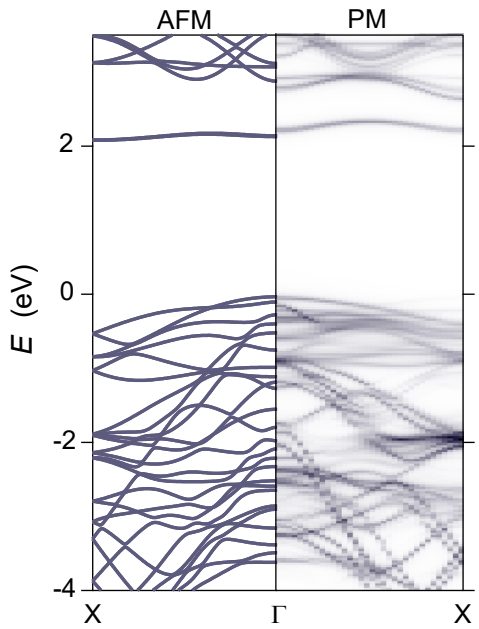


Supplementary Figure 7. **Direct comparison of AFM and PM calculations**. Here the calculations presented in Fig. 4 of the main text are presented without overlay of experimental data, and on a wider energy scale to include the conduction bands.

## Supplementary References

* matthew.watson@diamond.ac.uk


[1] D. Pescia, A. R. Law, M. T. Johnson, and H. P. Hughes, Determination of observable conduction band symmetry in angle-resolved electron spectroscopies: Non-symmorphic space groups, Solid State Communications **56**, 809 (1985).

[2] V. Arpiainen and M. Lindroos, Effect of Symmetry Distortions on Photoelectron Selection Rules and Spectra of $Bi_2Sr_2CaCu_2O_{8+\delta}$, Phys. Rev. Lett. **97**, 037601 (2006).

[3] M. Cattelan, C. J. Sayers, D. Wolverson, and E. Carpene, Site-Specific Symmetry Sensitivity of Angle-Resolved Photoemission Spectroscopy in Layered Palladium Diselenide, 2D Mater. **8**, 045036 (2021).

[4] V. Brouet, M. F. Jensen, P.-H. Lin, A. Taleb-Ibrahimi, P. Le Fèvre, F. Bertran, C.-H. Lin, W. Ku, A. Forget, and D. Colson, Impact of the Two Fe Unit Cell on the Electronic Structure Measured by ARPES in Iron Pnictides, Phys. Rev. B **86**, 075123 (2012).

[5] M. Bianchi, S. Acharya, F. Dirnberger, J. Klein, D. Pashov, K. Mosina, Z. Sofer, A. N. Rudenko, M. I. Katsnelson, M. van Schilfgaarde, M. Rösner, and P. Hofmann, Paramagnetic electronic structure of CrSBr: Comparison between ab initio GW theory and angle-resolved photoemission spectroscopy, Phys. Rev. B **107**, 235107 (2023).

[6] P. Blaha, K. Schwarz, F. Tran, R. Laskowski, G. K. H. Madsen, and L. D. Marks, WIEN2k: An APW+lo program for calculating the properties of solids, J. Chem. Phys. **152**, 074101 (2020).

[7] D. Koller, F. Tran, and P. Blaha, Improving the modified Becke-Johnson exchange potential, Phys. Rev. B **85**, 155109 (2012).

D. Pescia, A. R. Law, M. T. Johnson, and H. P. Hughes, De termination of observable conduction band symmetry in angle resolved electron spectroscopies: Non-symmorphic space groups, Solid State Communications 56, 809 (1985).
V. Arpiainen and M. Lindroos, Effect of Symmetry Dis tortions on Photoelectron Selection Rules and Spectra of $Bi_2Sr_2CaCu_2O_{8+\delta}$, Phys. Rev. Lett. 97, 037601 (2006).
M. Cattelan, C. J. Sayers, D. Wolverson, and E. Carpene, Site-Specific Symmetry Sensitivity of Angle-Resolved Photoemis sion Spectroscopy in Layered Palladium Diselenide, 2D Mater. 8, 045036 (2021).
V. Brouet, M. F. Jensen, P.-H. Lin, A. Taleb-Ibrahimi, P. Le Fevre, F. Bertran, C.-H. Lin,W. Ku, A. Forget, and D. Col784 son, Impact of the Two Fe Unit Cell on the Electronic Structure Measured by ARPES in Iron Pnictides, Phys. Rev. B 86, 075123 (2012).
L. Hedin, NewMethod for Calculating the One-Particle Green's Function with Application to the Electron-Gas Problem, Phys. Rev. 139, A796 (1965).
M. van Schilfgaarde, T. Kotani, and S. Faleev, Quasiparti cle Self-Consistent GW Theory, Phys. Rev. Lett. 96, 226402 (2006).
D. Pashov, S. Acharya, W. R. Lambrecht, J. Jackson, K. D. Belashchenko, A. Chantis, F. Jamet, and M. van Schilfgaarde, Questaal: A package of electronic structure methods based on the linear muffin-tin orbital technique, Computer Physics Com munications 249, 107065 (2020).
S. Acharya, D. Pashov, A. N. Rudenko, M. Rosner, M. van Schilfgaarde, and M. I. Katsnelson, Importance of charge self consistency in first-principles description of strongly correlated systems, npj Computational Materials 7, 208 (2021).
A. Zunger, S.-H.Wei, L. G. Ferreira, and J. E. Bernard, Special quasirandom structures, Phys. Rev. Lett. 65, 353 (1990).
T. G. Dargam, R. B. Capaz, and B. Koiller, Disorder and size effects in the envelope-function approximation, Phys. Rev. B 56, 9625 (1997).
P. V. C. Medeiros, S. Stafstrom, and J. Bjork, Effects of ex trinsic and intrinsic perturbations on the electronic structure of graphene: Retaining an effective primitive cell band structure by band unfolding, Phys. Rev. B, 89, 041407 (2014).
Z.Wang, X.-G. Zhao, R. Koch, S. J. L. Billinge, and A. Zunger, Understanding electronic peculiarities in tetragonal FeSe as l cal structural symmetry breaking, Phys. Rev. B 102, 235121 (2020).